

Effects of Anode Wettability and Slots on Anodic Bubble Behavior Using Transparent Aluminium Electrolytic Cells

ZHIBIN ZHAO,^{1,2} BINGLIANG GAO,^{1,3} YUQING FENG,² YIPENG HUANG,¹ ZHAOWEN WANG,¹ ZHONGNING SHI,¹ and XIANWEI HU¹

1.—School of Metallurgy, Northeastern University, Mail Box 117, Shenyang 110089, China
2.—CSIRO Mineral Resources, Clayton, VIC 3169, Australia. 3.—e-mail: blgao@mail.neu.edu.cn

Transparent aluminum electrolytic cells were used to study the effects of anode wettability and slots on bubble behavior in a similar environment to that used in industrial cells. Observations were conducted using two types of transparent cells, one with side-observation and the other with a bottom-observation cell design. Anodic bubbles rising process in the side channel is strongly affected by the wettability of the anode. After rising a short distance, the bubbles detach from the anode vertical surface at good-wetting anode cases, while the bubbles still attach to the vertical surface at poor-wetting anode cases. Anode slots of width of 4 mm are able to prevent smaller bubbles from coalescing into larger bubbles and thus decrease the bubble size and gas coverage on the anode. Anode slots also make a contribution in slightly reducing bubble thickness. With the presence of slots, the bubble-induced cell voltage oscillation decreases as well.

INTRODUCTION

Primary aluminum production is dominated by the Hall–Héroult process since its invention in 1886. Although the aluminum electrolytic technology has progressed enormously in the past decades, it is still one of the most energy intensive metallurgical processes utilized in modern industries. The Hall–Héroult process requires approximately 13,000 kWh electricity to extract 1 ton aluminum metal from alumina. However, the energy efficiency of this process is no higher than 50%, the rest of the energy being emitted to the atmosphere as waste heat. Therefore, it is very important to develop new technologies to reduce energy input and improve the energy efficiency for the aluminum reduction process. The most practical way may be to minimize the cell voltage while maintaining an optimal current efficiency.

The theoretical decomposition voltage for the reduction of alumina to aluminum cannot be further reduced as a back electromotive force of 1.756 V is necessary.¹ However, there are large opportunities to reduce voltage drops in other cell components since the total voltage drop is 4.0–4.6 V through the whole cell.¹ Potential ways to achieve a reduction of cell voltage may rely on the following directions:

- (a) Reduce the contact voltage drop, for example by improving the quality of the anode joints or optimizing the contact between the cathode block and the collect bars;
- (b) Improve the electrical conductivity of the electrolyte, carbon or other materials to reduce the ohmic voltage drop;
- (c) Reduce the voltage drop of the electrolyte layer in ‘the anode to cathode distance (ACD)’, for example by stabilizing the magneto-hydrodynamic (MHD) waves on the bath–metal interface, reducing the gas coverage or thickness at the anodes, and accelerating bubble releasing from the anode bottom.

The most promising direction is reducing the voltage drop in ACD, which contributes one-third of the cell voltage. The ACD voltage drop is about 1.344 V through a spacing of 40 mm,¹ corresponding to an average voltage drop of about 33.6 mV/mm in this spacing. The cell voltage drop would be significantly reduced if the ACD is decreased.

A significant limitation in reducing ACD is due to the anodic bubbles adhering to the anode bottom surface. In a typical aluminum reduction cell, the carbon anodes are consumed at a rate of 1.5 cm per day,² which is caused by the chemical reaction

between carbon and atomic oxygen with a product of CO_2 gas emission (0.002 m^3 per s in 1 m^2).² The anodic gas is dispersed as bubbles in the molten salt, which slide along the anode bottom until they are released at the anode edges, and rise in the side channel of the cell. It has been reported that the gas coverage on the anode surface ranges from 24% to 90%³ and the bubbles thickness is about 5 mm.⁴ The presence of these bubbles is not only an obstacle in reducing ACD but also results in an extra voltage drop due to its high electrical resistivity. Recently, a numerical study⁵ pointed out that the position and coverage of anodic bubbles even influences the horizontal current distribution in the metal pad. A positive attribution is that the bubble motion drives the bath flow,^{6–8} which has great impacts on alumina dispersion.^{9,10} In order to minimize their negative effects and ultimately maximize their benefits, a better understanding of anodic bubbles is necessary.

Due to the restrictions of high temperature and the heavily corrosive environment of the molten cryolite, such a study would be extremely difficult to conduct in industrial cells, particularly for obtaining detailed bubble dynamics. Consequently, physical models are necessary substitutive methods, which have been reviewed in the literature.^{4,11} These studies provided valuable information in improving our understanding of anodic bubbles. However, there are two significant differences between physical models and real CO_2 -cryolite electrochemical systems: (1) the physicochemical properties of fluid media and construction materials; and (2) the mechanism of gas generation. Despite being an intensive research area, the detailed understanding of bubble behavior has not yet been conclusively elucidated. It is necessary to investigate the behavior of anodic bubbles in actual industrial cell environments and operational parameters.

In this consideration, transparent aluminum electrolytic cells, also called ‘see-through cells’, have been developed by several research teams, e.g., Haupin et al.,^{12,13} Qiu et al.,^{14–17} Utigard et al.,^{18,19} Keller et al.,²⁰ Cassayer et al.,^{21,22} Xue et al.,²³ and Gao et al.^{24,25} The construction diagrams of transparent aluminum electrolytic cells are shown in the supplementary material.

The current paper presents a study of the bubble behavior in two types of transparent aluminum electrolytic cells, in particular how the bubble rising process in the side channel varies with the wettability of the anode vertical surface. The effect of longitudinal and transverse slots on the anodes was also assessed in terms of bubble morphology, gas coverage and the resultant cell voltage oscillation.

Experiment Setup and Image Processing

Experiment Setup

The experiments were conducted using two types of transparent aluminum electrolytic cells developed at Northeastern University: the side-

observation transparent aluminum electrolytic cell developed by Qiu et al.,¹⁴ and the bottom-observation transparent aluminum electrolytic cell developed by Zhao et al.²⁵

Side-Observation Transparent Aluminum Electrolytic Cell

Figure 1 shows the schematic diagram of the side-observation transparent aluminum electrolytic cell. Both anode and cathode were put into a single-chamber silica crucible. Two types of anodes were studied in this cell. Anode 1 was bare and anode 2 was shielded by a quartz tube. The purpose of this experiment was to assess the effect of anode wettability on bubble behavior in the side channel of the cell.

The anode was suspended 10 mm above the cathode, which was lying on the bottom of the quartz crucible. The electrolyte depth was 40 mm and the anode current density was set to 0.7 A/cm^2 . The bubble behavior was recorded at a speed of 15 frames per s (FPS) from one side window of the cell by an industrial camera (MV-VS078FC).

Bottom-Observation Transparent Aluminum Electrolytic Cell

Because the cathode was positioned under the anode, it was not possible to observe the bubble behavior in the ACD using the side-observation transparent aluminum electrolytic cell. Thus, a bottom-observation transparent aluminum electrolytic cell was developed as shown in Fig. 2. The crucible design was correspondently improved from single-chamber to double-chamber as shown in Fig. 3. This design allows the anode and cathode to be put into separate chambers. The two chambers were connected by a 1-mm gap at the bottom of the

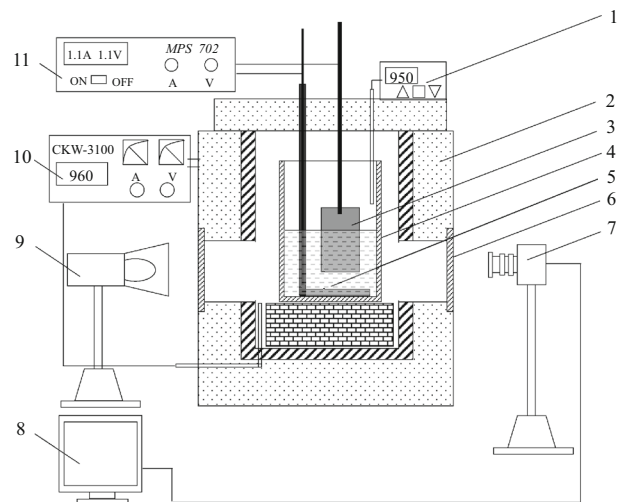


Fig. 1. The schematic diagram of the side-observation transparent aluminum electrolytic cell 1 Thermocouple; 2 furnace; 3 anode; 4 quartz crucible; 5 cathode; 6 side-observation quartz window; 7 high-speed camera; 8 computer; 9 light source; 10 mps 3100 temperature controller; 11 702 DC power supply.

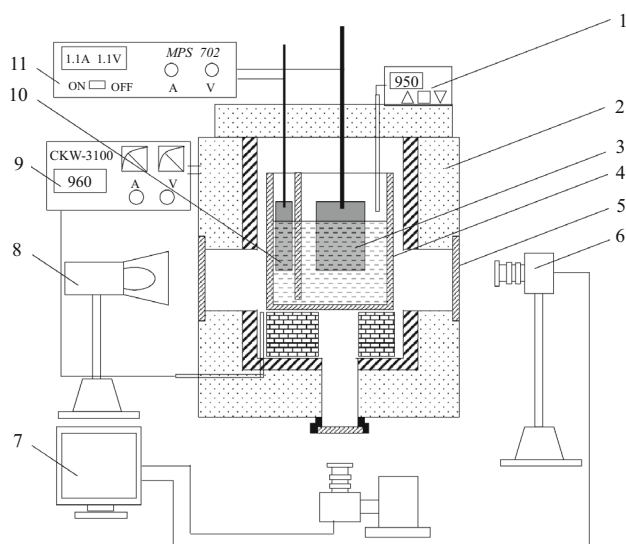


Fig. 2. The schematic diagram of the bottom-observation transparent aluminum electrolytic cell. 1 Thermocouple; 2 furnace; 3 anode; 4 quartz crucible; 5 bottom-observation quartz window; 6 industrial camera; 7 computer; 8 light source; 9 mps 3100 temperature controller; 10 cathode; 11 702 DC power supply.

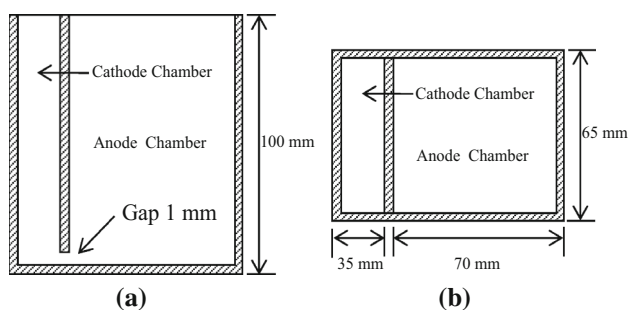


Fig. 3. The double-chamber quartz crucible. (a) Front view, (b) top view.

middle wall, which allowed the current to flow from the anode to the cathode. In order to show the cell diagram clearly, the quartz crucible was horizontally rotated by 90° to illustrate the cross-section in Fig. 2.

Using this transparent cell, three types of anodes (anodes 3, 4 and 5) were used to study the effect of anode design on bubble behavior. These anodes were designed with the same size (length 50 mm, width 22 mm, height 70 mm) with/without slots on the bottom:

- Anode 3 was a traditional unslotted anode as a base case;
- Anode 4 had one longitudinal slot (width 4 mm, length 50 mm and depth 15 mm);
- Anode 5 had two transverse slots (width 4 mm, length 22 mm and depth 15 mm).

According to the equation given by Hartland et al.,²⁶ the maximum thickness of a growing CO_2 bubble on the downward facing plate is 2.8 mm. As the slot width should be larger than this value, 4 mm was chosen here as the width of slots. The anode bottom surface was divided into uniform parts with slots.

The anode and cathode were suspended 30 mm above the crucible bottom in separate chambers of the double-chamber quartz crucible. The immersion depth of anode was 40 mm. The anodic current density applied was set in the range of $0.3\text{--}1.3\text{ A/cm}^2$ with an interval of 0.2 A/cm^2 . The bubble behavior was captured simultaneously from the bottom window and the side window by two industrial cameras (MV-VS078FC, 15FPS). The corresponding cell voltage during electrolysis was recorded by an Agilent HP34401A Digital MultiMeter.

In this study, all anodes and cathodes were made of high-purity graphite, and the schematic diagrams and the purposes of five types of anodes are briefly summarized in Fig. 4 and Table I.

The composition of the electrolyte used in these experiments was based on a cryolite mixture (NaF 45.7 wt.%, AlF_3 41.8 wt.%, LiF 5 wt.%, CaF_2 4 wt.%, Al_2O_3 3.5 wt.%). All chemicals were dried at 673 K for more than 3 h and stored in a dry container before use. The furnace temperature was controlled at $1223 \pm 5\text{ K}$ by an MPS3100 Temperature Controller.

Image Processing

Image processing was applied to obtain detailed bubble information, e.g., bubble dynamics, bubble boundary and gas coverage. As this was well described in our previous work,⁴ only a brief introduction is given here.

The images were first dissected from the experimental videos by frames. In the software Image Pro-Plus 6.0, the bubble edge was marked by a yellow line and each bubble was identified by a unique ID number. Figure 5 shows an example of images before and after image processing.

The cover area of each bubble under the anode bottom was calculated based on the image pixel information. The instantaneous coverage was calculated by the following equation:

$$\varphi = \frac{\sum_{i=1}^I S_i}{a \times b} \quad (1)$$

where φ is the instantaneous gas coverage; I is the total number of bubbles appearing in the instantaneous image; i is the bubble ID; S_i is the area of the i th bubble; and a and b are the length and width of the anode bottom surface, respectively.

The average coverage at a fixed current density was calculated by the following equation:

$$\bar{\varphi} = \frac{1}{J} \sum_{j=1}^J \varphi_j \quad (2)$$

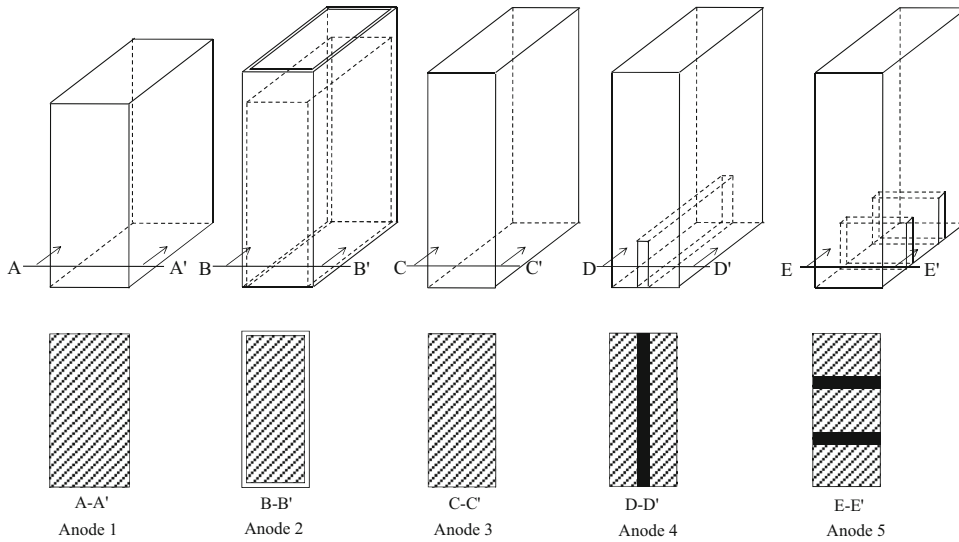


Fig. 4. Schematic diagrams of the five anode designs.

Table I. List of experiments conducted in this paper

Cell design	Anode	Anode configurations(mm)	Purposes
Side-observation cell	Anode 1	Rectangle (26 × 50 × 50)	The effect of anode vertical surface wettability on bubble rising
	Anode 2	Rectangle (20 × 50 × 50), shielded by quartz tube	
Bottom-observation cell	Anode 3	Rectangle (22 × 50 × 70)	The effect of slots on bubble morphology, gas coverage, bubble thickness and voltage oscillation
	Anode 4	Rectangle (22 × 50 × 70), with one longitudinal slot (4 × 50)	
	Anode 5	Rectangle (22 × 50 × 70), with two transverse slots (4 × 22)	

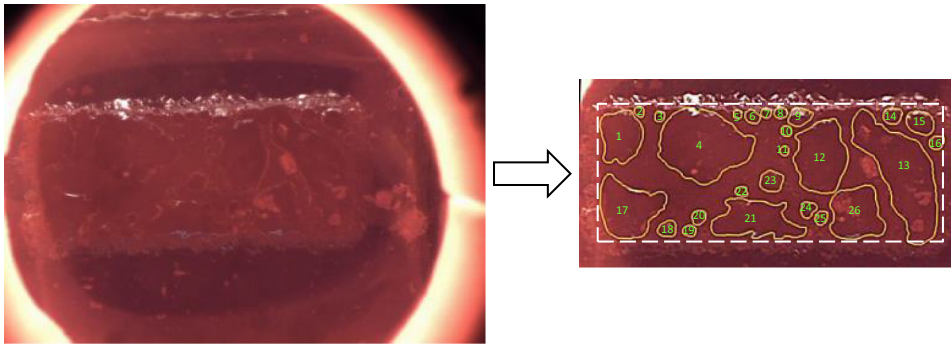


Fig. 5. Gas bubbles on the anode surface before and after image processing.

where $\bar{\varphi}$ is the average coverage of all images at the fixed current density; J is the total number of images at the fixed current density; j is the image ID; and φ_j is the instantaneous coverage of the j th image.

Due to the resolution of the images, only bubbles greater than 0.5 mm in diameter were analyzed.

RESULTS AND DISCUSSION

Effect of Wettability of the Anode Vertical Surface

It is clear that the rising motion of bubbles in the side channel is an important momentum source for the circulation of the bath flow. In addition to the

buoyancy force and drag force, the wettability of the anode vertical surface also plays an important role on the rising bubbles.

Wetting property characterizes the degree of liquid spreading on the solid in equilibrium with a vapor phase. It is quantified by the contact angle. Up to now, the contact angle of aluminum electrolyte on graphite or carbon surface has been well studied. Although researchers show a small difference in the exact value of the contact angle, it is widely accepted that it is well above 90° (shown in Table II; 180° = no wetting and 0° = complete wetting). This means the electrolyte shows poor wetting on the carbon anode. In order to assess the wettability of the electrolyte on quartz materials, a sessile drop experiment was carried out. The experimental setup was similar to that used in a previous work,²⁷ and is not given here. An electrolyte particle (about 2 g) was placed on a quartz plate, and the morphological changes were recorded by a camera. The results are shown in Fig. 6. It can be seen that the liquid electrolyte completely wetted the quartz plate during the particle melting, which indicated that the quartz plate was strongly wetted by the electrolyte. Therefore, anode 1 and anode 2 were considered reasonable to represent the cases with poor wetting and good wetting, respectively.

The bubble evolutions beneath anode 1 and anode 2 are similar, which has been well reported in both transparent aluminum electrolytic cells^{4,12,23} and water models.^{3,31,32} It is not necessary to repeat this investigation here, so only the different bubble behaviors after entering into the side channel will be discussed in this section.

Figure 7 shows the bubble rising morphologies along the anode vertical surfaces with different wettability. The difference can be clearly seen: on the poor-wetting anode 1, the rising big bubble adheres to the vertical surface and climbs towards the electrolyte surface, as shown in Fig. 7a. In the case of the good-wetting anode 2 in Fig. 7b, the big bubble detaches from the vertical surface after rising a short distance, and then the bubble moves freely in the liquid and finally releases from the liquid surface. It is interesting to note that the bubble rising behavior along the good-wetting anode

2 is similar to air bubbles rising in the water model; for instance, both the CO_2 bubble and the air bubble detach from the anode vertical surface after a short distance of climbing.^{11,33} The similar wettability of solid to liquid in the two systems contributes to this similarity.

Water models are now widely applied in studying bubble dynamics and the related phenomena. Our previous work³³ numerically investigated the dominant factors affecting the bubble dynamics differences between air–water and real CO_2 -cryolite systems. It was found that the wetting of the electrolyte on the anode dominates differences in the bubble dynamics. Here, the experiments conducted on anodes with different wettability in the real CO_2 -cryolite system reconfirmed our previous conclusion.

Effect of Anode Slots

Slotted anodes are a well-accepted technology for energy saving in the aluminum electrolytic process. Some applications are given in Table III.

However, the results for the application of slotted anodes have not always been positive due to the obvious negative aspects, and in some instances there do exist examples of failure.⁴⁰ The detailed understanding of the effect of anode slots is not fully clear, and the design for these slots is still made empirically in modern aluminum smelters.

In the following sections, the energy-saving mechanism of longitudinal or transverse slots will be discussed in terms of bubble morphology, gas coverage, bubble thickness, and bubble-induced voltage oscillation.

Bubble Morphology

Bottom Observations

Figure 8 shows some characteristic bubble morphologies in a bubble life cycle at the fixed current density of 0.9 A/cm^2 . It appears that the slot divides the entire anode surface into separated parts: the longitudinal slot divides the original anode (aspect ratio 2.27) into two slim parts (aspect ratio 5.56 for each part), and the two transverse slots divide the

Table II. The contact angle of cryolite electrolyte on graphite reported in the literature

Contact angle($^\circ$)	Alumina (wt.%)	Atmosphere	Temp. (K)	Method	Refs.
110–130	4	–	–	Transparent cell	23
103.4	5	Air	1223	Sessile drop	27
100–135	0–10	N_2	1273	Sessile drop	28
124–141	0–6	N_2	–	Sessile drop	29
105	0–3	N_2	1303	Sessile drop	30

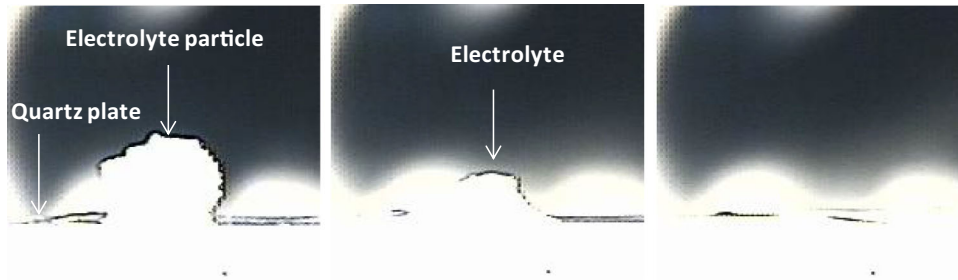


Fig. 6. The wettability measurement of the electrolyte on quartz material.

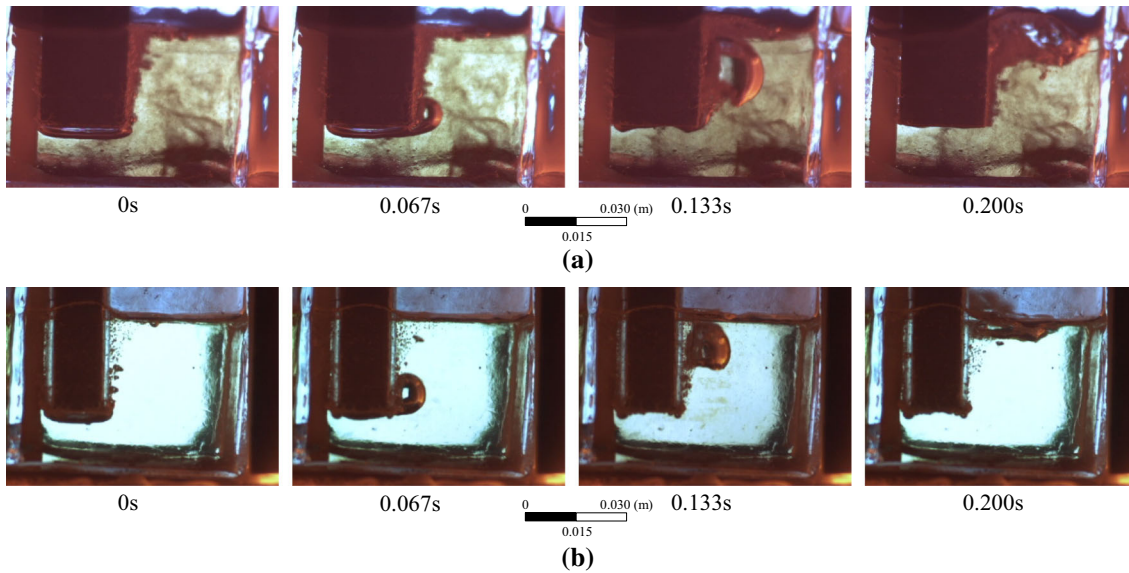


Fig. 7. Anodic gas bubbles rising along anode vertical surfaces with different wettability: (a) anode 1 for the poor-wetting case, (b) anode 2 for the good-wetting case.

Table III. The applications of slotted anodes in commercial aluminum electrolytic cells

PLANTS	Slots (mm), number	Positive aspects			Negative aspects
		Cell voltage (mV)	Current efficiency	Energy saving (kWh/t Al)	
Alcoa ³⁴	–	↓150	↑0.5%	–	Anode consumption↑
Hydro ³⁵	1L (15 × (130 – 160))	↓30	–	–	Dust generation↑
Rio Tinto ³⁶	2 L	↓35–66	–	–	Spiking↑
ALBRAS ³⁷	2 T	↓17	–	↓297	Fe in metal↑
Hindalco ³⁸	2 L (13 × 100)	↓107	–	↓348	Operational problems↑
R&D Carbon ³⁹	2 L (12 × 150)	↓18	–	–	
	2 L (12 × 300)	↓35			
	2 T (12 × 150)	↓10			
	2 T (12 × 300)	↓20			
ELKEM ⁴⁰	–	–	↓1.0%	–	

L longitudinal, *T* transverse.

original anode (aspect ratio 2.27) into three parts (aspect ratio 1.57 for each part). On the unslotted anode, the bubbles coalesce into larger bubbles as they make contact with each other, as shown in Fig. 8a. However, it is interesting to notice the bubbles on slotted anodes cannot move through the slots for further coalescence. The unslotted anode leads to the maximum bubble size among the three types of anodes, the transverse slots significantly decrease it, and the longitudinal slot makes a further reduction. These observations indicate that the slot of a width of 4 mm is able to prevent bubbles from coalescing into larger bubbles and allows the release of smaller bubbles from slotted anodes. While the common slot width in industrial cells is now around 10–15 mm,⁴¹ the current investigation provides valuable evidence for possible use of a narrower slot width in a real cell, though more work is needed to optimize the slot width on an industrial scale.

Figure 9 illustrates the situations of gas coverage on the three types of anodes. The gas coverage presents a cyclical fluctuation behavior over all three anode designs. The only difference is that the fluctuation frequency is higher for slotted anodes. Apparently, the slots make for faster bubble releasing and smaller bubble size from the anode bottom.

Figure 10 shows the relationship of gas coverage and current density on the three types of anodes. The current density ranges from 0.3 A/cm² to 1.3 A/cm². The curves represent the average coverage. The solid symbols and the hollow symbols are the maximum and the minimum coverage, respectively. The curves of both slotted anodes as well as the unslotted anode in these experiments show that higher current density leads to lower average/maximum gas coverage, which has not been reported in the literature.

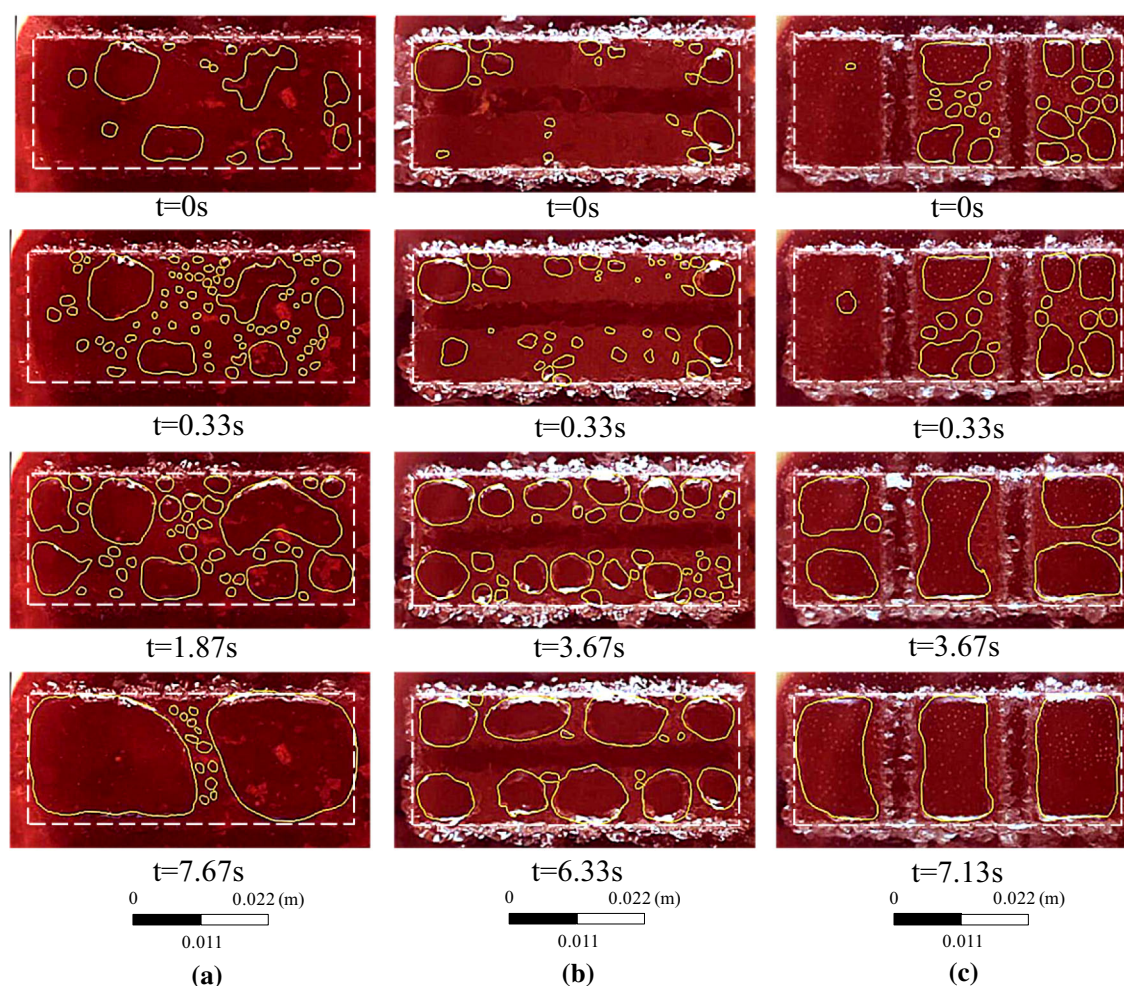


Fig. 8. Bottom view of the characteristic bubble morphologies for three types of anodes at current density of 0.9 A/cm². (a) Anode 3 for the unslotted case, (b) anode 4 for the longitudinally slotted case, (c) anode 5 for the transversely slotted case.

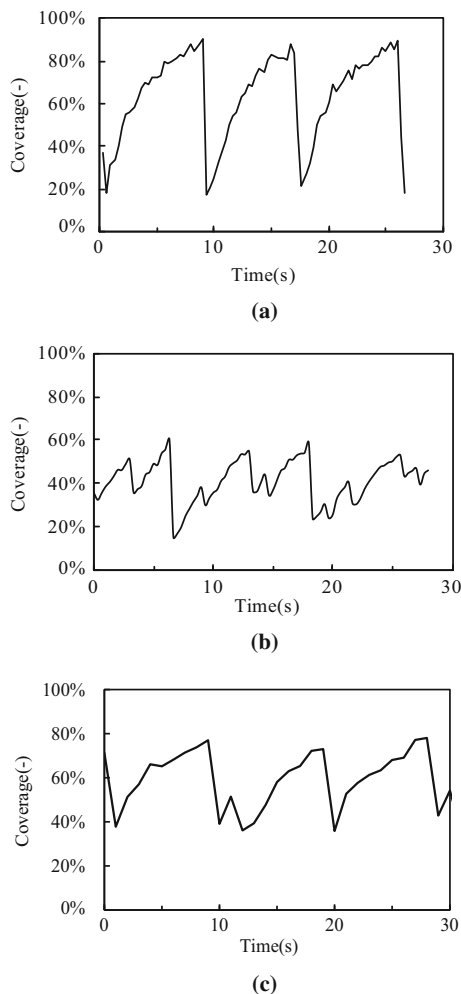


Fig. 9. The fluctuation of gas coverage at current density of 0.9 A/cm^2 . (a) Anode 3 for the unslotted case, (b) anode 4 for the longitudinally slotted case, (c) anode 5 for the transversely slotted case.

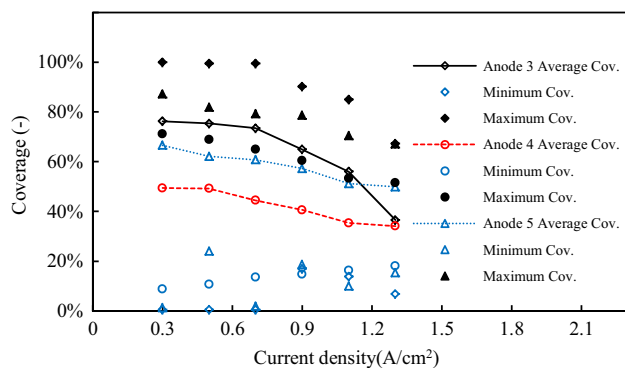


Fig. 10. Gas coverage on anodes versus current densities for the unslotted anode and slotted anodes (anode 3 for the unslotted case, anode 4 for the longitudinally slotted case, anode 5 for the transversely slotted case).

Another indication from Fig. 10 is that the maximum and average gas coverage on slotted anodes are much lower than that on the unslotted anode under the same conditions (same current density and same ACD, etc.).

We previously tested the rationality of the double-chamber design based on the unslotted anode using the CFD model,⁴ in which the non-uniform current density on the anode bottom was acceptable in the view of observing the bubble behavior. Anode 4 has a similar design as anode 3 and the bubble behavior also shows a similar phenomenon. However, the defect of the double-chamber design is amplified in the experiment performed with anode 5. The current prefers to flow out from the part of the anode close to the cathode (the right part of the anode bottom in Fig. 8c). During the electrolysis, the near-cathode part is preferred for generating gas bubbles. After the near-cathode part was partly covered by bubbles, gas bubbles began to appear on the far-cathode part (the left part of the anode bottom in Fig. 8c). An improved design of this quartz crucible is necessary for the future study of the transversely slotted anode.

Side Observations

In addition to the bottom view, the side bubble morphologies (as shown in Fig. 11) were viewed from one side window of the transparent cell. Combined with the bottom view, it is helpful to clearly illustrate the three-dimensional bubble evolutions. For a better comparison, the bubble morphologies of both the side view in Fig. 11 and bottom view in Fig. 8 were taken simultaneously. As the presence of the bubble layer is an obstacle in preventing further reduction of ACD, it is interesting to check whether the slots contribute to the reduction of bubble layer thickness and ACD. The evolution of the bubble layer thickness was measured according to image processing in the period of 2–3 bubble life cycles and plotted in Fig. 12.

Similar to the gas coverage, the evolution of bubble layer thickness shows a cyclic pattern. In the cases of low aspect ratio anodes (unslotted anode 3 and transversely slotted anode 5), the bubble thickness shows a clear periodic pattern, which is not obvious on the high aspect ratio anode, e.g., the longitudinally slotted anode 4.

The maximum measured bubble thickness is 4.5 mm on the unslotted anode, and it is decreased slightly by the presence of slots. These results demonstrate that the slots make a contribution in reducing the thickness of the bubble layer and could allow a reduction in ACD, although the contribution is small.

In this experiment, we cannot see the bubbles collected in the slots from the bottom view in Fig. 8. However, it can be clearly seen from the side observations that there is continuous bubbling from the slots. Even in the slots of anode 5, the gathering of gas bubbles in the slots can be clearly observed in Fig. 11c. This result is consistent with the observations of a low-temperature electrolytic cell

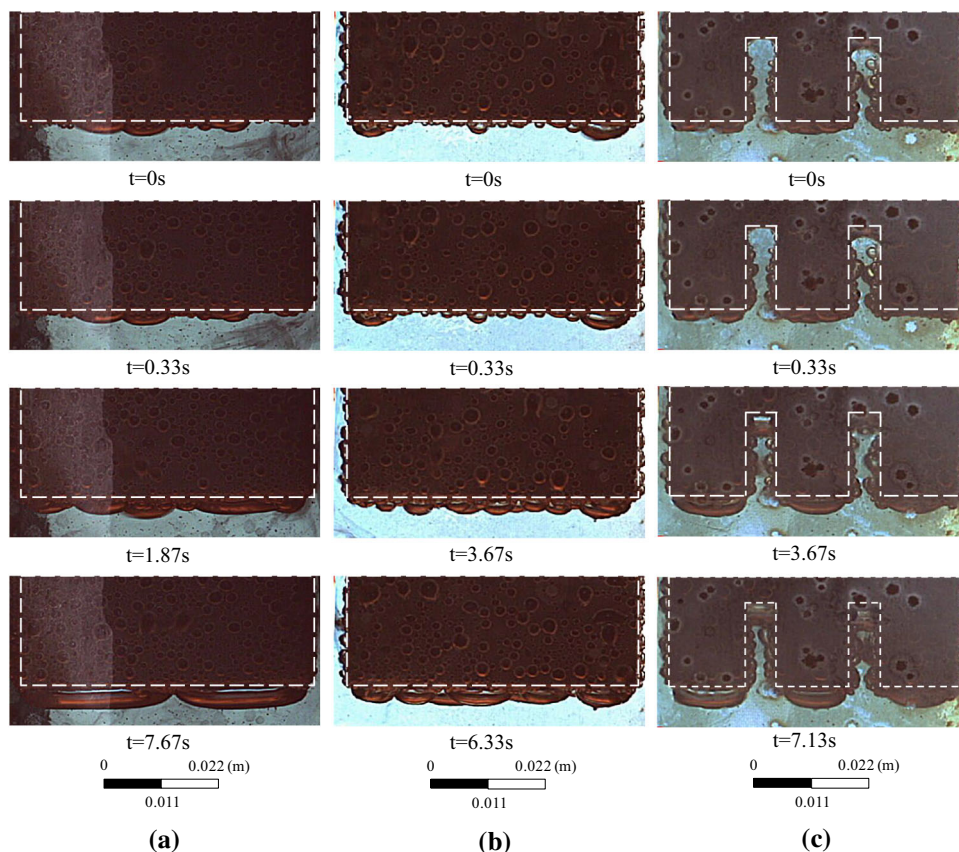


Fig. 11. Side view of the characteristic bubble thickness for the three types of anodes at current density of 0.9 A/cm^2 . (a) Anode 3 for the unslotted case, (b) anode 4 for the longitudinally slotted case, (c) anode 5 for the transversely slotted case.

conducted by Chen et al.,⁴² who demonstrated that the bubbles are easily collected and coalesced in the ‘valleys’, and released from these ‘valleys’.

Bubble-Induced Voltage Oscillation

The bubble-induced voltage oscillation represents the difference in cell voltage with gas bubbles present (high voltage) and gas release (low voltage), which can be calculated by Eqs. 3 and 4.

$$V_{\text{ave}} = \frac{\sum_{m=1}^M |V_m|}{M} \quad (3)$$

$$V_{\text{oscillation}} = \frac{\sum_{m=1}^M |V_m - V_{\text{ave}}|}{M} \quad (4)$$

where V_m refers to the m th cell voltage datum, and M is the total number of cell voltage data; V_{ave} is the average value of cell voltage; and $V_{\text{oscillation}}$ is the average oscillation of cell voltage.

In this section, the comparisons of the unslotted anode 3 and the longitudinally slotted anode 4 are acceptable due to the similar anode design. As the design of the transversely slotted anode 5 causes uneven current density distribution on the anode

bottom, which may affect the comparison of voltage oscillation, the comparison with anode 5 should not be over-interpreted.

Figure 13 shows the trends of the cell voltage oscillation with current density for three types of anodes. At all current densities, the cell voltage oscillation on the slotted anodes is smaller than that on the unslotted anode. When operating at an anodic current density of 0.9 A/cm^2 , the average cell voltage oscillation has a magnitude of 24.5 mV on the unslotted anode, while it is 15.5 mV on anode 4 and 16.0 mV on anode 5, corresponding to a reduction rate of 36.7% and 34.7%, respectively. This figure shows that the slot technology is beneficial for reducing the oscillation of cell voltage, which plays a positive role in energy saving and cell stability.

It is interesting to note that the highest current density does not lead to the largest voltage oscillation according to this study. The cell voltage oscillation initially increases with increasing current density and decreases later at higher current density for all three types of anodes. If this is true within industrial cells, higher current densities could be a benefit to the cell stability.

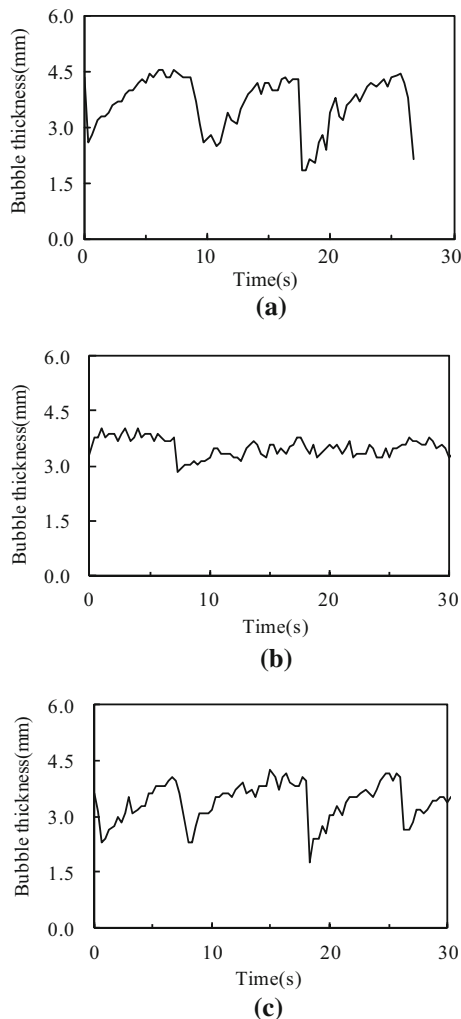


Fig. 12. The fluctuation of bubble layer thickness at current density of 0.9 A/cm^2 . (a) Anode 3 for the unslotted case, (b) anode 4 for the longitudinally slotted case, (c) anode 5 for the transversely slotted case.

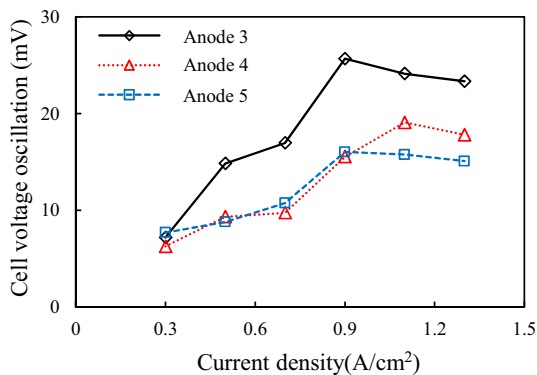


Fig. 13. The magnitude of cell voltage oscillation at different current densities for the unslotted anode and slotted anodes (anode 3 for the unslotted case, anode 4 for the longitudinally slotted case, anode 5 for the transversely slotted case).

CONCLUSION

Anodic gas bubble behavior on five graphite anodes with different designs were studied using high-temperature transparent electrolytic cells in a real CO_2 -cryolite system. The effects of anode wettability and anode slots on bubble dynamics and cell voltage have been discussed in detail.

The main findings from this study are:

- (1) For the side-observation experiments, the rising bubble adheres to the vertical surface of the poor-wetting anode and climbs towards the electrolyte surface; conversely, the bubble detaches from the vertical surface after rising a short distance along the good-wetting anode.
- (2) The above results, with the same cell operating system but different wettability of solid to liquid, reconfirm the previous numerical conclusion that the wettability dominates the difference in bubble dynamics between the air–water and real CO_2 -cryolite systems. This finding is helpful in selecting substitutive systems.
- (3) For the bottom-observation experiments, the maximum bubble size and gas coverage decrease with the presence of slots, especially for the longitudinally slotted anode. Slots of 4 mm in width are able to prevent bubbles crossing them and allow the release of smaller bubbles from these slots.
- (4) The bubble layer thickness shows a similar cyclic pattern with gas coverage. The maximum bubble thickness is about 4–5 mm, and it decreases slightly under the two slotted anodes.
- (5) At all current densities, anode slots decrease the oscillations of cell voltage. At a current density of 0.9 A/cm^2 , the average oscillation of the cell voltage is about 24.5 mV for the unslotted anode, while it decreases to 15.5 mV for the longitudinally slotted anode and to 16 mV for the transversely slotted anode.

ACKNOWLEDGEMENTS

The authors would like to express their gratitude for the financial support by the National Natural Science Foundation of China (Grant Nos. 51322406, 51434005, 51474060, 51574070 and 51529401). Zhibin Zhao would also like to thank the China Scholarship Council (CSC) for a visiting PhD scholarship to CSIRO in Australia.

ELECTRONIC SUPPLEMENTARY MATERIAL

The online version of this article (doi:[10.1007/s11837-016-1999-6](https://doi.org/10.1007/s11837-016-1999-6)) contains supplementary material, which is available to authorized users.

REFERENCES

1. H. Kvande and W. Haupin, *JOM* 53, 29 (2001).
2. J. Zoric and A. Solheim, *J. Appl. Electrochem.* 30, 787 (2000).
3. S. Fortin, M. Gerhardt, and A.J. Gesing, *Light Metals 1984*, ed. J.P. McGeer (Warrendale, PA: TMS, 1984), pp. 385–395.
4. Z. Zhao, Z. Wang, B. Gao, Y. Feng, Z. Shi, and X. Hu, *Metall. Mater. Trans. B* 47, 1962 (2016).
5. W. Tao, T. Li, Z. Wang, B. Gao, Z. Shi, X. Hu, and J. Cui, *JOM* 68, 600 (2015).
6. A. Solheim, S.T. Jonansen, and S. Rolseth, *J. Appl. Electrochem.* 19, 703 (1989).
7. T. Haarberg, A. Solheim, and S.T. Johansen, *Light Metals 1998*, ed. B. Welch (San Francisco, PA: TMS, 1998), pp. 475–481.
8. Y. Feng, M.P. Schwarz, W. Yang, and M. Cooksey, *Metall. Mater. Trans. B* 46, 1956 (2015).
9. Y. Feng, M.A. Cooksey, and M.P. Schwarz, *Light Metals 2011*, ed. S.J. Lindsay (Warrendale, PA: TMS, 2011), pp. 543–548.
10. H. Zhang, S. Yang, H. Zhang, J. Li, and Y. Xu, *JOM* 66, 1210 (2014).
11. K. Zhang, Y. Feng, M.P. Schwarz, Z. Wang, and M.A. Cooksey, *Ind. Eng. Chem. Res.* 52, 11378 (2013).
12. W.E. Haupin and W.C. McGrew, *Light Metals 1974*, ed. H. Forberg (Warrendale, PA: TMS, 1974), pp. 37–47.
13. W.E. Haupin and W.C. McGrew, *Aluminium* 51, 273 (1975).
14. Z. Qiu, L. Fan, and K. Grjotheim, *Light Metals 1986*, ed. R.E. Miller (Warrendale, PA: TMS, 1986), pp. 525–533.
15. Z. Qiu, L. Fan, N. Feng, K. Grjotheim, and H. Kvande, *Light Metals 1987*, ed. R.D. Zabreznik (Warrendale, PA: TMS, 1987), pp. 409–416.
16. Z. Qiu and M. Zhang, *Electrochim. Acta* 32, 607 (1987).
17. Z. Qiu, L. Fan, K. Grjotheim, and H. Kvande, *J. Appl. Electrochem.* 17, 707 (1987).
18. T. Utigard and J.M. Toguri, *Light Metals 1986*, ed. R.E. Miller (Warrendale, PA: TMS, 1986), pp. 405–413.
19. T.A. Utigard, J.M. Toguri, and S.W. Ip, *Light Metals 1988*, ed. L.G. Boxall (Warrendale, PA: TMS, 1988), pp. 703–706.
20. R. Keller and K.T. Larimer, *Light Metals 1992*, ed. E. Cutshall (Warrendale, PA: TMS, 1992), pp. 464–467.
21. L. Cassayre, T.A. Utigard, and S. Bouvet, *JOM* 54, 41 (2002).
22. L. Cassayre, G. Plascencia, T. Marin, S. Fan, and T.A. Utigard, *Light Metals 2006*, ed. T.J. Galloway (Warrendale, PA: TMS, 2006), pp. 379–383.
23. J. Xue and H.A. Oye, *Light Metals 1992*, ed. E. Cutshall (Warrendale, PA: TMS, 1992), pp. 265–271.
24. B. Gao, X. Hu, J. Xu, Z. Shi, Z. Wang, and Z. Qiu, *Light Metals 2006*, ed. T.J. Galloway (Warrendale, PA: TMS, 2006), pp. 467–470.
25. Z. Zhao, Z. Wang, B. Gao, Y. Feng, Z. Shi, and X. Hu, *Light Metals 2015*, ed. M. Hyland (Warrendale, PA: TMS, 2015), pp. 801–806.
26. S. Hartland and R.W. Hartley, *Axisymmetric fluid-liquid interfaces: tables giving the shape of sessile and pendant drops and external menisci, with examples of their use*, 1st ed. (New York: Elsevier Scientific Publishing Co., 1976).
27. S. Liu, W. Li, Y. Ban, and Z. Wang, *China Nonferr. Metall.* 6, 20 (2008).
28. P. Meunier and B. Welch, *J. Appl. Electrochem.* 39, 837 (2009).
29. J.B. Metson, R.G. Haverkamp, M.M. Hyland, and J. Chen, *Light Metals 2002*, ed. W. Schneider (Warrendale, PA: TMS, 2002), pp. 239–244.
30. E. Lae, V. Sahajwalla, B. Welch, and M. Skyllas-Kazacos, *J. Appl. Electrochem.* 35, 199 (2005).
31. K. Vékony and L.I. Kiss, *Metall. Mater. Trans. B* 43B, 1086 (2012).
32. Y. Wang, L. Zhang, and X. Zuo, *Metall. Mater. Trans. B* 42B, 1051 (2011).
33. Z. Zhao, K. Zhang, Y. Feng, P. Witt, P. Schwarz, Z. Wang, and M.A. Cooksey, Melbourne, Australia, unpublished research, 2014.
34. X. Wang, G. Tarcy, S. Whelan, S. Porto, C. Ritter, B. Ouellet, G. Homley, A. Morphet, G. Proulx, S. Lindsay, and J. Bruggeman, *Light Metals 2007*, ed. M. SØrlie (Warrendale, PA: TMS, 2007), pp. 539–544.
35. H. Gudbrandsen, N. Richards, S. Rolseth, and J. Thonstard, *Light Metals 2003*, ed. P.N. Creapeau (Warrendale, PA: TMS, 2003), pp. 323–327.
36. G. Bearne, D. Gadd, and S. Lix, *Light Metals 2007*, ed. M. SØrlie (Warrendale, PA: TMS, 2007), pp. 305–310.
37. H.P. Dias and R.R. Moura, *Light Metals 2005*, ed. H. Kvande (Warrendale, PA: TMS, 2005), pp. 341–344.
38. S.C. Tandon and R.N. Prasad, *Light Metals 2005*, ed. H. Kvande (Warrendale, PA: TMS, 2005), pp. 303–309.
39. M.W. Meier, R.C. Perruchoud, and W.K. Fischer, *Light Metals 2007*, ed. M. SØrlie (Warrendale, PA: TMS, 2007), pp. 277–282.
40. K.A. Rye, E. Myrvold, and I. Solberg, *Light Metals 2007*, ed. M. SØrlie (Warrendale, PA: TMS, 2007), pp. 293–298.
41. F. Yan, M. Dupuis, J. Zhou, and S. Ruan, *Light Metals 2013*, ed. B. Sadler (Warrendale, PA: TMS, 2013), pp. 537–542.
42. J.J.J. Chen, K. Qian, and J. Zhao, *Chem. Eng. Res. Des.* 79, 383 (2001).